Metal-insulator transition of $(SrIrO_3)_1/(NdNiO_3)_3$ superlattice under strain

Yiren Liu,[1,2] Xu Li [1,2] Jun-Ming Liu,[1] and Yurong Yang[1,2,*]

[1]*National Laboratory of Solid State Microstructures, Nanjing University, Nanjing 210093, China*

[2]*Jiangsu Key Laboratory of Artificial Functional Materials, Department of Materials Science and Engineering, Nanjing University, Nanjing 210093, China*

We investigate the magnetic and electronic properties of strongly correlated perovskite $(SrIrO_3)_1/(NdNiO_3)_3$ superlattice by density-functional theory calculations. The semiconducting ground state of the superlattice adopts a metal-insulator transition (MIT) under compressive epitaxial strain. This MIT is induced by the large reduction of breathing distortion and octahedra antiferrodistortive distortion in the superlattice compared to the $NdNiO_3$ under epitaxial strain. Furthermore, it is found that this breathing distortion couples to the T-type antiferromagnetic ordering with two types of magnetic order on Ni sublattices, leading to a magnetic state without the degenerate switched magnetic direction when the breathing distortion is unchanged. Our results provide a mechanism of MIT in superlattice and a possible way to tune the magnetic order by breathing distortion.

I. INTRODUCTION

Transition-metal oxides exhibit rich phase diagrams, including different forms of electronic order (charge, orbital, magnetic) and metal-insulator transitions (MITs) [1,2], which are fundamental paradigms of modern condensed-matter physics and are essential for recently proposed device applications. Many transition-metal oxides can undergo MIT triggered by chemical composition, spin-orbital ordering, temperature, strain, and other methods [3–7]. The strong electron correlations in transition-metal oxides are believed to be related to high-temperature superconductivity [8,9], colossal magnetoresistance [10,11], next-generation neuromorphic computing [12,13], and other important and potentially useful phenomena. Rare-earth nickelates ($RNiO_3$, R = rare earth), including bulk and thin films and heterostructures, have recently attracted large interest [14,15], because of the interesting MIT (apart from $LaNiO_3$) [16–20] and various potential applications [21]. The MIT in $RNiO_3$ compounds concurrently occurs with a structure phase transition from orthorhombic $Pbnm$ in the high-temperature metallic phase to monoclinic $P2_1/n$ in the low-temperature insulating phase [22–25]. This symmetry lowering from high-temperature phase to low-temperature phase is accompanied by the appearance of a breathing distortion of the oxygen octahedra with expanded and compressed NiO_6 octahedra arranged in rocksalt-like pattern. In addition, for $RNiO_3$ with $\underline{R}$ = Nd and Pr, the Néel temperature is equal to the metal-insulator transition temperature and $RNiO_3$ compounds go directly from paramagnetic metal to antiferromagnetic (AFM) insulator (spin order identified by a Bragg vector q =(1/4, 1/4, 1/4) in pseudocubic notation) [26,27]. The magnetic moments vary

between Ni atoms in the center of expanded octahedra and compressed octahedra [28,29] and the interplay between the breathing distortion and magnetic ordering has been studied based on density-functional theory [30,31].

Understanding the underlying mechanism of the MIT is a crucial subject of condensed-matter physics, however, which is still a subject not fully understood. This difficulty in fully understanding MIT and strong electron correlation usually gives rise to complex many-body phenomena and close coupling of charge, spin, orbital, and lattice degrees of freedom. Identification of the important key interactions that influence the metal-insulator transitions in correlated materials has consequently remained elusive.

Here, by means of first-principles calculations, we investigate electronic and magnetic properties in $(SrIrO_3)_1/(NdNiO_3)_3$ (SIO_1/NNO_3) superlattice. Our results reveal that the ground state of SIO_1/NNO_3 superlattice is characterized by a semiconducting T-type AFM state with a split of the electronic states of two different Ni sublattices. A MIT occurs in SIO_1/NNO_3 superlattice under compressive strain, which is structurally triggered by the reduction of octahedra antiferrodistortive (AFD) distortions and breathing distortion. We furthermore find the interplay between breathing distortion and the complex AFM ordering.

Computational method

First-principles calculations were performed within the density-functional theory, as implemented in the Vienna *ab initio* Simulation Package [32,33]. An energy cutoff of 550 eV was used, and the set of projector-augmented wave potentials [34,35] was employed to describe the electron-ion interaction. Valence electron configurations, $4s^2 4p^6 5s^2$ for Sr, $5d^8 6s^1$ for Ir, $5s^2 5p^6 6s^2$ for Nd (the extra $4f$ electrons are frozen in the pseudopotentials), $3d^8 4s^2$ for Ni, and $2s^2 2p^4$ for O were considered. Electronic relaxations converged within 10^{-7} eV

*yangyr@nju.edu.cn

054113-1
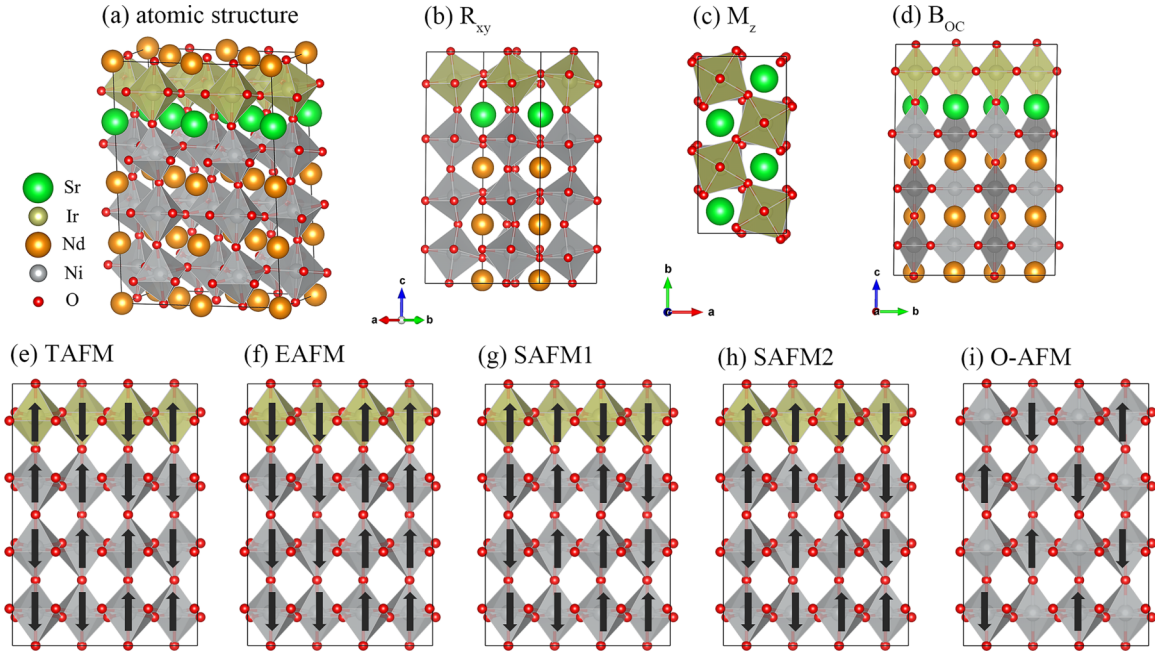
FIG. 1. Sketch of the atomic structure, lattice distortions, and complex colinear antiferromagnetic orderings. (a) Atomic structure of SIO_1/NNO_3 superlattice. (b) Antiphase rotations of oxygen octahedra about [100] and [010] direction (R_{xy}). (c) In-phase rotations of oxygen octahedra about [001] direction (M_z). (d) Breathing distortion of the O_6 octahedra in Ni sublattices (B_{OC}). (e) T-type AFM, (f) E-type AFM, (g) S-AFM1, and (h) S-AFM2 orderings. (i) The ground-state AFM ordering in bulk NdNiO$_3$ (O-AFM). The green, yellow, orange, gray, and red spheres represent the Sr, Ir, Nd, Ni, and O atoms, respectively.

and ionic relaxation was performed until the residual force was less than 1 meV/Å. We used the Perdew-Burke-Ernzerhof parametrization revised for solids (PBEsol) functional with Hubbard U correction [36–38] (selecting $U = 2$ eV for Ir [39,40] and $U = 2$ eV for Ni [18,41]) for electronic structure calculations. Recently, Binci et al. [42] proposed density-functional theory (DFT)$+U+V$ approach. This fully ab initio methodology can also describe the rare-earth nickelates correctly and capture the features well established by experimental characterizations. A $\sqrt{2} \times 2\sqrt{2} \times 4$ supercell with 80 atoms was used [shown in Fig. 1(a)], and a Γ-centered $6 \times 3 \times 2$ k-point mesh was adopted. Different magnetic orderings, including ferromagnetic (FM), and complex T-type, E-type, and S-type AFM orderings, were considered [shown in Figs. 1(e)–1(i)]. Symmetry-adapted mode analysis allowing the extraction of lattice-distortion amplitudes has been performed with the BILBAO crystallographic server [43,44]. The modes are normalized to their amplitude in the T-type AFM ground state.

II. RESULTS

A. Magnetic and electronic properties

We study the stability of AFM orderings in NdNiO$_3$ (NNO) and SIO_1/NNO_3 superlattice first. Different AFM configurations are considered. As shown in Fig. 1, T-type, E-type, and S-type orderings, which are based on $\uparrow\uparrow\downarrow\downarrow$ spin chains in the (**ab**) plane with different stackings along the c axis, are considered in our calculations. In NNO, the initial settings of S-type AFM and T-type AFM ordering will be optimized to O-AFM ordering. The oxygen octahedron without a black arrow indicates that the magnetic moment of the Ni atom in the octahedron is 0. Figure 2 shows the energy differences
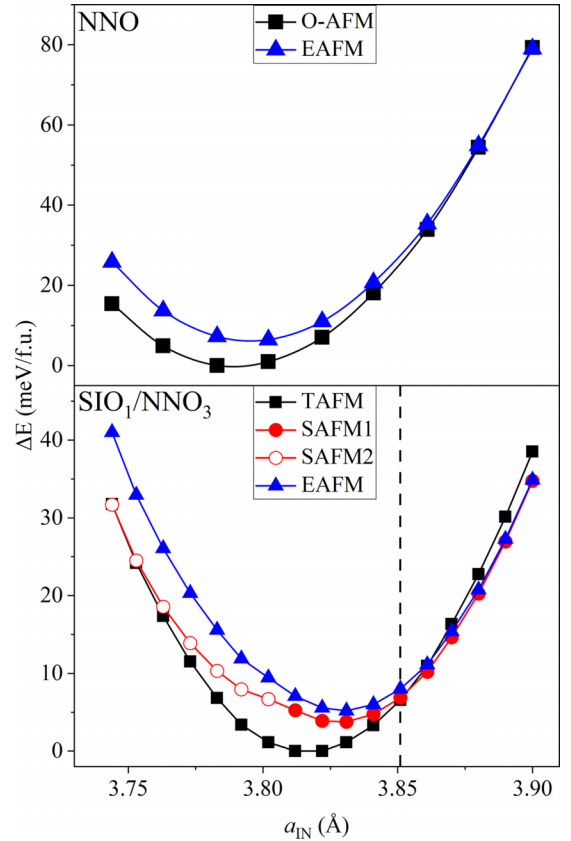
FIG. 2. Energy differences of different magnetic orders for SIO_1/NNO_3 superlattice (bottom panel) and NNO (top panel) as a function of in-plane lattice constant (a_{IN}).

TABLE I. The in-plane lattice constants correspond to ground state, magnetic phase transition from T-AFM to S-AFM, magnetic phase transition from S-AFM1 to S-AFM2, largest band gap, and MIT in SIO_1/NNO_3 superlattice.

	Ground state	T-AFM to S-AFM	S-AFM1 to S-AFM2	Largest band gap	MIT
a_{IN}(Å)	3.822	3.851	3.802	3.851	3.755

of different magnetic structures as a function of a_{IN}. The in-plane lattice constants corresponding to ground state, magnetic phase transition from TAFM to SAFM, magnetic phase transition from SAFM1 to SAFM2, largest band gap, and MIT in SIO_1/NNO_3 superlattice are summarized in Table I. The a_{IN} of the ground state of SIO_1/NNO_3 superlattice (3.822 Å) is larger than that of NNO (3.783 Å) since the lattice constant of bulk $SrIrO_3$ is larger than that of bulk NNO. In NNO, the O-AFM ordering is lower in energy than E-type AFM ordering and is always the ground state within the considered range of epitaxial strain. While in SIO_1/NNO_3 superlattice, the T-type AFM ordering is favored when the a_{IN} is smaller than 3.851 Å and the S-type AFM ordering becomes more energetically favorable than T-type AFM ordering when the a_{IN} is larger than 3.851 Å, implying a magnetic phase transition from S-type AFM to T-type AFM. The E-type AFM ordering is higher in energy over the whole range of epitaxial strain. Note that S-type AFM has two configurations, namely S-AFM1 and S-AFM2, and only the magnetic order in the second layer (close to SIO layer) is different. There is a magnetic phase transition from S-AFM1 to S-AFM2 occurring at a_{IN} = 3.802 Å. S-AFM1 is more stable when a_{IN} is larger than 3.802 Å while it is S-AFM2 when a_{IN} is smaller than 3.802 Å. We also study the SIO_2/NNO_2 superlattice. The 2/2 superlattice has metal ground state and keeps metal state when in-plane lattice constant is within the range of 3.82 to 3.90 Å, which indicates that there is no MIT in 2/2 superlattice.

It is noteworthy that the energy difference for tensile strain in the superlattice case is quite small, which is a reliable result. Taking the $BiFeO_3$ (BFO) as an example, MacDougall et $al.$ [45] showed evidence for phase coexistence of G-type and C-type antiferromagnetic-order parameters in T-like monoclinic phase of BFO in experiments. Diéguez et $al.$ [46] showed that energy splitting between the C-AFM and G-AFM ordering is about 5 meV/f.u. in T phase of BFO (c/a aspect ratios approaching 1.3) based on first-principle calculations, which is quite small. As for rare-earth nickelates, Varignon et $al.$ [18] showed that the energy difference between S-AFM and T-AFM ordering is 0.5 meV/f.u. in $NdNiO_3$. We believe that the energy differences of several meV per formula unit between different magnetic orderings under tensile strain in the superlattice may yield a reliable result.

We also study electronic structures of SIO_1/NNO_3 superlattice. Figure 3 shows the band gap of SIO_1/NNO_3 superlattice with T-type AFM and S-type AFM ordering as a function of a_{IN}, together with the band gap of ground phase of NNO for comparison. One can see that the band-gap of NNO is always larger than that of SIO_1/NNO_3 superlattice in all considered epitaxial strains. To distinguish the ground state and metastable state, we use open and solid symbols to represent band gaps for metastable and ground states, respectively, in Fig. 3. Superlattice with T-AFM ordering possesses

the largest band gap when a_{IN} is 3.851 Å, and superlattice with S-AFM ordering possesses the largest band gap when a_{IN} is 3.831 Å. NNO has the largest band gap when a_{IN} is 3.822 Å. When a_{IN} is smaller than 3.755 Å for superlattice with T-AFM ordering, the band gap is zero, implying that MIT occurs when a_{IN} is 3.755 Å. When a_{IN} is smaller than 3.802 Å for superlattice with S-AFM ordering, the band gap is zero, which is consistent with the magnetic transition from S-AFM1 to S-AFM2 at a_{IN} = 3.802 Å. In contrast, the band gap is always nonzero for all the considered epitaxial strains for NNO.

The electronic structures are investigated to find out the details of MIT of SIO_1/NNO_3 superlattice. The d_{xy}, d_{yz}, and d_{xz} orbitals of Ni ions are fully occupied for NNO and superlattice. Figure 4 shows the projected density of states of e_g states from Ni ions. The top panels and bottom panels show the projected density of states of e_g orbitals of Ni sublattice located within the center of shrunken and expanded O_6 octahedra (denoted as Ni_1 and Ni_2), respectively. Figures 4(a) and 4(b) display the projected density of states of $Ni-e_g$ states of NNO at a_{IN} = 3.783 Å and the insulating state of SIO_1/NNO_3 superlattice at a_{IN} = 3.822 Å, respectively. One clearly sees the band gap is 0.46 eV for NNO and 0.14 eV for superlattice. From the total amount of occupied valence states [Figs. 4(b) and 4(c)], Ni_1 occupies many more e_g electrons than Ni_2. Figure 4(c) shows the projected density of states of $Ni-e_g$ states of the metallic state of SIO_1/NNO_3 superlattice at a_{IN} = 3.744 Å. The d_{z^2} and $d_{x^2-y^2}$ orbitals cross the Fermi level and the projected density of states for spin-up state and spin-down state are asymmetric, explicating that the net magnetic moment in the metal state is nonzero.
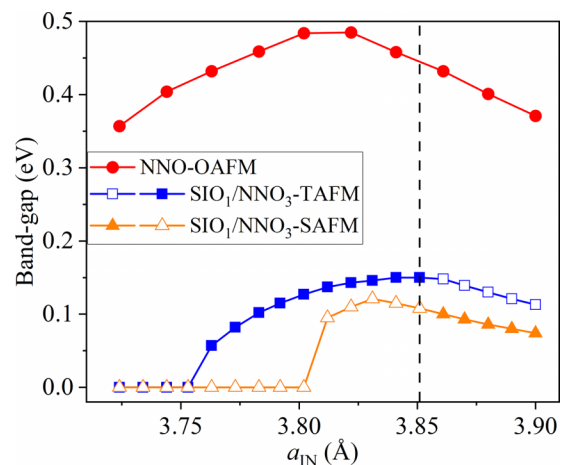
FIG. 3. Band gaps of NNO and SIO_1/NNO_3 as a function of a_{IN}. The open and solid symbols represent the metastable and ground states.
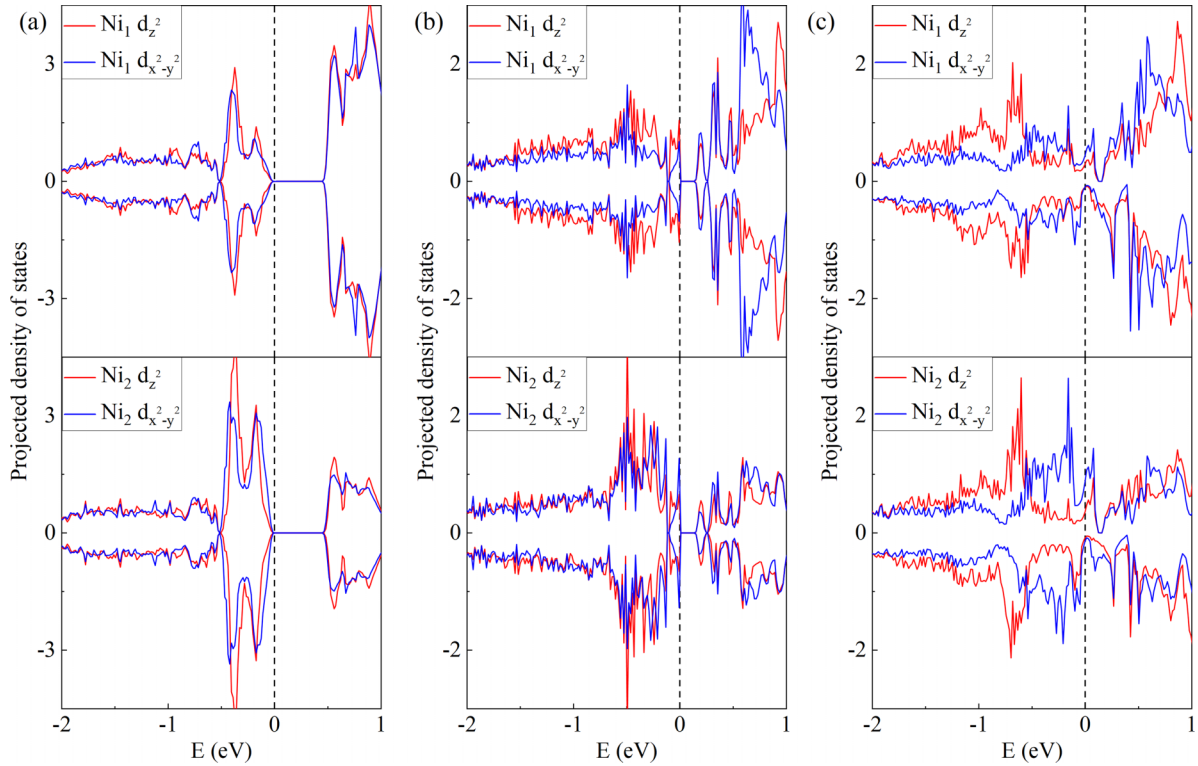
FIG. 4. Projected density of states of Ni$-e_g$ states of (a) NNO at $a_{\text{IN}} = 3.783$ Å, (b) insulating state of SIO$_1$/NNO$_3$ at $a_{\text{IN}} = 3.822$ Å, and (c) metallic state of SIO$_1$/NNO$_3$ superlattice at $a_{\text{IN}} = 3.744$ Å. Projected density of states of the e_g states for Ni ions with the shrinking O$_6$ octahedron centered (Ni$_1$) and the expanding O$_6$ octahedron centered (Ni$_2$) are shown in the top panel and bottom panel, respectively.

Let us now investigate the charge and magnetic moment of Ni atoms and Ir atoms in SIO$_1$/NNO$_3$ superlattice. The magnetic moments of Ir atoms and Ni atoms in SrIrO$_3$, NdNiO$_3$, metal state of SIO$_1$/NNO$_3$, and insulator state of SIO$_1$/NNO$_3$ are summarized in Table II. Take the first NiO$_2$ layer as an example: for the insulating state at $a_{\text{IN}} = 3.822$ Å, there are two Ni$_1$ ions with atomic charge of $9.41e$ and magnetic moment of 0.53 μB, while the other two Ni$_2$ ions possess atomic charge of $9.24e$ and magnetic moment of 1.23 μB, and these two kinds of Ni sublattices are arranged alternately along [100] and [010] directions. The SIO layer of SIO$_1$/NNO$_3$ superlattice will restrain the contraction and expansion of the NiO$_6$ octahedron along [001] direction. For metallic state at $a_{\text{IN}} = 3.744$ Å, there are two Ni$_1$ atoms with charge of $9.41e$ and magnetic moment of 0.74 μB, while the other two Ni$_2$ atoms possess charge of $9.34e$ and a magnetic moment of 1.02 μB. Differences in the amount of charge and magnetic moment between the two types of Ni sublattices diminish as the a_{IN} decreases, which further confirms that B_{OC} distortion in SIO$_1$/NNO$_3$ superlattice subsides during the MIT. Compared to the ground state of NNO, the magnetic moment of Ni$_2$ ions is 1.19 μB, which is very close

to that in SIO$_1$/NNO$_3$ superlattice. The magnetic moment of Ni$_1$ ions is nearly null in NNO and the magnetic moment of Ni$_1$ in SIO$_1$/NNO$_3$ superlattice is much larger, which illuminates charge transfer from Ir atoms to Ni atoms. It is noteworthy that our computed magnetic moments on both Ni sublattices appear to be in contradiction with the conclusion of the charge analysis. This contradiction can be explained by the fact that Ni$_1$ cations receive a significant fraction of electrons coming from the surrounding oxygens which are weakly spin polarized. The details of the contradiction are investigated in Ref. [18]. For the IrO$_2$ layer in the insulator state, four Ir atoms both have magnetic moment of 0.79 μB, indicating that the B_{OC} distortion is nearly null in the IrO$_2$ layer. As a result of the charge transfer from Ir atoms to Ni atoms, Ir cations have larger magnetic moment than that of bulk SrIrO$_3$ (0.35 μB). Ir cations have atomic charge of $8.38e$ in the insulator state and have atomic charge of $8.45e$ in the metal state, which demonstrates that charge transfer from Ir atoms to Ni atoms weakens when transitioning from insulator to metal. SrIrO$_3$ layer plays two roles in MIT in (SrIrO$_3$)$_1$/(NdNiO$_3$)$_3$ superlattice. First, the bulk SrIrO$_3$ is metallic, making MIT in (SrIrO$_3$)$_1$/(NdNiO$_3$)$_3$ superlattice

TABLE II. Magnetic moment of Ir atoms and Ni atoms in SrIrO$_3$, NdNiO$_3$, metal state of SIO$_1$/NNO$_3$, and insulator state of SIO$_1$/NNO$_3$.

	SrIrO$_3$	NdNiO$_3$	SIO$_1$/NNO$_3$(metal)	SIO$_1$/NNO$_3$(insulator)
m_{Ir}/μB	0.35		0.66	0.79
m_{Ni}/μB		1.19/0	0.74/1.02	0.53/1.23
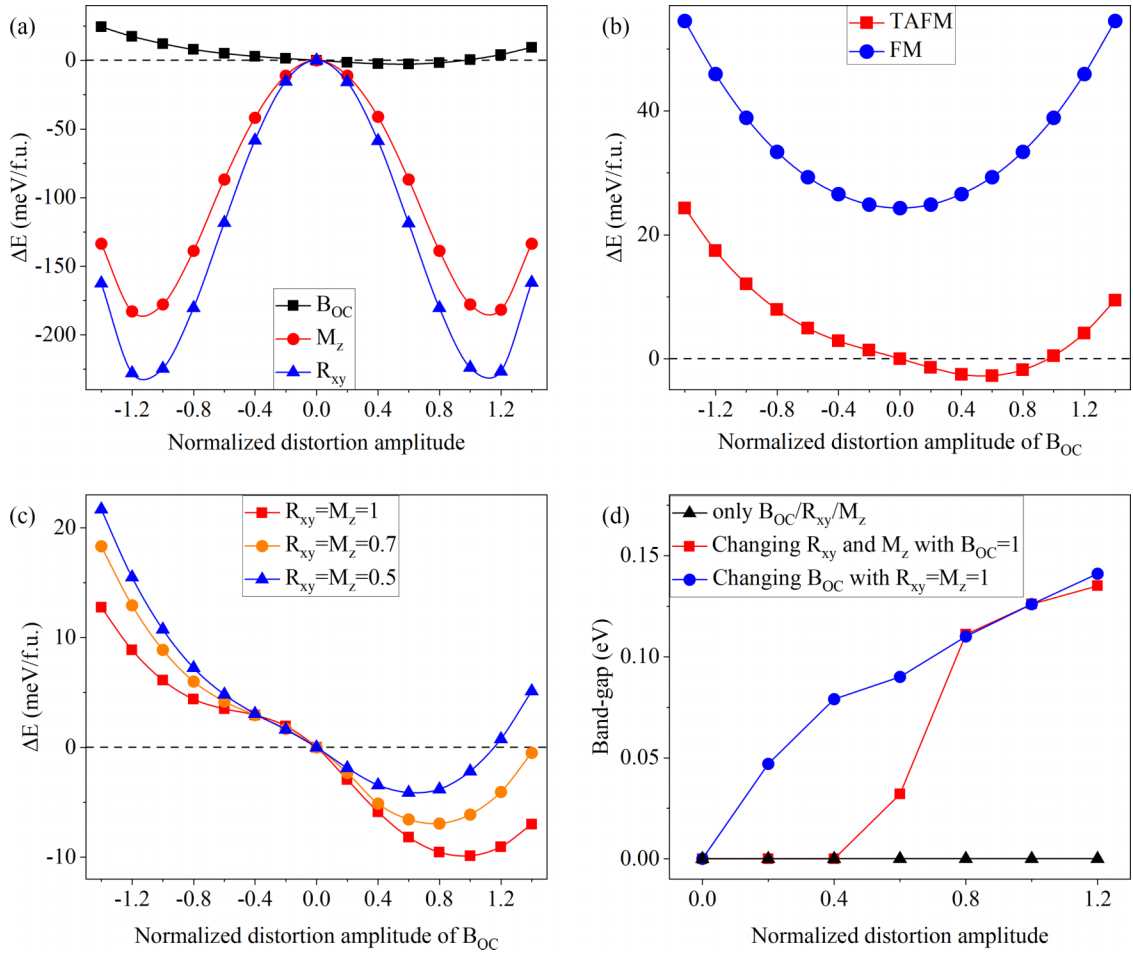
FIG. 5. (a) Energies of SIO_1/NNO_3 superlattice with T-AFM ordering and no strain as functions of normalized-distortion amplitude of lattice distortion of B_{OC}, R_{xy}, and M_z. The high-symmetry structure without any lattice distortion is the structure with zero normalized-distortion amplitude. (b) Energies of SIO_1/NNO_3 with T-AFM and FM orderings as a function of amplitude of B_{OC} distortion. (c) Energies of SIO_1/NNO_3 as a function of amplitude of B_{OC} distortion when freezing different amplitudes of R_{xy} and M_z distortion. (d) Band gaps of SIO_1/NNO_3 as a function of amplitude of single distortion ($B_{OC}/R_{xy}/M_z$) (black triangles), amplitude of $R_{xy} = M_z$ when fixing $B_{OC} = 1$ with (red squares), as well as amplitude of B_{OC} distortion when fixing $R_{xy} = M_z = 1$ (blue circles).

much more possible to occur. Second, charge transfer from Ir atoms to Ni atoms can suppress the breathing distortion in NdNiO₃ layers, which makes the band gap of NdNiO₃ layers become smaller and even closed. We will analyze the impact of breathing distortion on the MIT in detail later. We also perform DFT + U + SOC calculations for ground state and metallic state of $(SrIrO_3)_1/(NdNiO_3)_3$ superlattice. We find that the impacts of spin-orbit coupling (SOC) on magnetic moment and charge transfer from Ir atoms to Ni atoms are very small. Therefore, strong SOC is not important for the MIT effect in superlattices.

B. Structural distortions of the ground state

To understand the effects of structural distortions on the electronic properties, we now investigate the structural distortions compared to the high-symmetry perovskite structure with space group of $P4mm$. As shown in Figs. 1(b)–1(d), the SIO_1/NNO_3 superlattice possesses three main lattice distortions, namely in-plane antiphase oxygen octahedra AFD distortions (R_{xy}), out-of-plane in-phase oxygen octahedra

AFD distortions (M_z), and a breathing distortion of the O₆ octahedra in Ni sublattices (B_{OC}) which results in two different Ni sublattices. As illustrated in Fig. 5(a), R_{xy} and M_z of SIO_1/NNO_3 with T-AFM show large instabilities and a large energy gain when their amplitudes are nonzero, resulting in characteristic symmetric double-well potentials. These wells remain double-well shape for all considered magnetic order. In contrast, the B_{OC} distortion possesses a single-well shape of energy-distortion curve, rather than a double-well curve, which indicates that a positive sign of B_{OC} is stable rather than a negative sign of B_{OC}. The single-well shape also indicates a coupling between the B_{OC} distortion and T-AFM order. Figure 5(b) shows the energy of the superlattice with T-AFM order as a function of amplitude of B_{OC} distortion, as well as that with FM magnetic order. One can confirm that the energy of the FM order is higher than the T-AFM order and shows a symmetric single well.

We further analyze the interplay between B_{OC} distortion and AFM ordering. Considering that there are two inequivalent Ni sublattices in SIO_1/NNO_3 superlattice, we can use two spin vectors $\mathbf{S_1}$ and $\mathbf{S_2}$ to characterize the spins on Ni₁
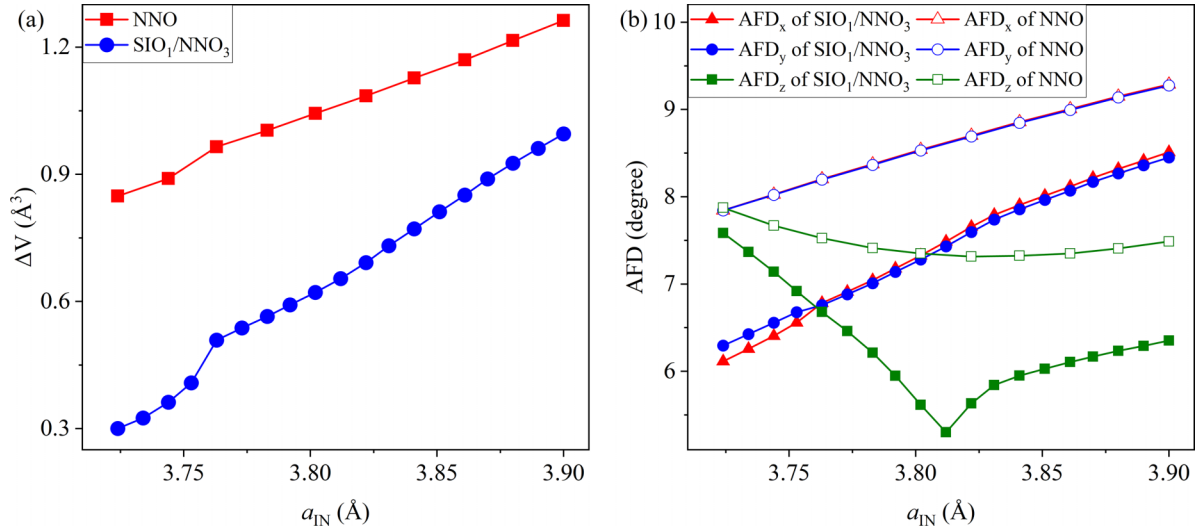
FIG. 6. (a) The differences in volume between expanding NiO_6 octahedra and shrinking NiO_6 octahedra as a function of the a_{IN} for NNO and SIO_1/NNO_3 superlattice. (b) AFD distortions of NiO_6 octahedra about x, y, and z axes as a function of a_{IN} for NNO and SIO_1/NNO_3 superlattice.

and Ni_2 sublattices, respectively. S_1 and S_2 are themselves three-dimensional spin vectors. S_1 and S_2 can be combined to form a complex vector $\psi = S_1 - iS_2$, which is actually the Fourier coefficient of the spin-density wave. There are two inequivalent AFM orderings, namely $\psi_1 = S_1 - iS_2$ and $\psi_2 = S_1 + iS_2$. The coupling between B_{OC} distortion and T-AFM ordering can be given by $S_1 \cdot S_2 \cdot B_{OC}$, which leads to asymmetric single-well energy as a function of B_{OC} distortion. Therefore, the structure with ψ_1 magnetic ordering and $+1$ B_{OC} is degenerate with the structure with ψ_2 magnetic ordering and -1 B_{OC}. This coupling between B_{OC} distortion and complex AFM ordering is not found in classical simple magnetic ordering (namely A-, C-, and G-type AFM and FM). The interplay between B_{OC} distortions and the complex AFM order also has been found in rare-earth nickelates, namely the T-AFM ordering becomes energetically more favorable due to the suppression of the NiO_6 octahedron with the onset of the breathing-mode distortion [31].

Figure 5(c) shows the energy of SIO_1/NNO_3 superlattice as a function of the amplitude of B_{OC} distortion with freezing R_{xy} and M_z at three different amplitudes, namely $R_{xy} = M_z = 1, 0.7$, and 0.5. It is single well for the very small $R_{xy} = M_z$ [$R_{xy} = M_z = 0$ in Fig. 5(b) and $R_{xy} = M_z = 0.5$ in Fig. 5(c)], while the curves turn to asymmetric double well when $R_{xy} = M_z = 0.7$ and 1 [Fig. 5(c)]. We also calculate the energy associated with B_{OC} distortion with freezing R_{xy} and M_z distortion in FM ordering, which exhibits a symmetric single-well shape. The single-well shape in FM ordering illustrates that the asymmetric double-well shape in T-AFM ordering is caused by the interplay between B_{OC} distortion and the T-AFM ordering instead of a trilinear coupling between B_{OC}, R_{xy}, and M_z distortions.

To reveal the impact of different distortions on the band gap, Fig. 5(d) displays the band gaps as a function of the amplitude of lattice distortion. One can clearly see that SIO_1/NNO_3 superlattice remains in a metal state when considering one single distortion (R_{xy}, M_z, or B_{OC}) increasing individually. Figure 5(d) also displays the

band gaps as a function of the amplitude of $R_{xy} = M_z$ when condensing $B_{OC} = 1$ (which is the magnitude of the ground state). The band gap of SIO_1/NNO_3 superlattice opens when the amplitude of R_{xy} and M_z distortions are larger than 0.4 and increases with the increase of the amplitude of $R_{xy} = M_z$. Figure 5(d) further displays the band gaps as a function of the amplitude of B_{OC} distortion when fixing $R_{xy} = M_z = 1$ (the magnitude of R_{xy} and M_z is that in the ground state). Band gap of SIO_1/NNO_3 superlattice opens when B_{OC} distortion is nonzero, and increases when the amplitude of B_{OC} distortion increases. These results indicate that the MIT in SIO_1/NNO_3 superlattice is induced by the decreasing of R_{xy}, M_z, and B_{OC} distortion.

C. Evolution of structural distortions during metal-insulator transition

We then consider the structural distortions of NNO and SIO_1/NNO_3 superlattice under epitaxial strain. Figure 6(a) shows the volume difference between the Ni_1-site octahedron and the Ni_2-site octahedron as a function of a_{IN}, which indicates the magnitude of B_{OC} distortion. B_{OC} distortion of NNO and SIO_1/NNO_3 superlattice decreases with the decrease of a_{IN}. B_{OC} distortion of NNO is always larger than that of SIO_1/NNO_3 superlattice, which is consistent with the larger band gap of NNO than SIO_1/NNO_3 superlattice (Fig. 3). B_{OC} distortion of SIO_1/NNO_3 superlattice exhibits a sharp drop at $a_{IN} = 3.753$ Å, which is consistent with MIT at $a_{IN} = 3.753$ Å and the fact that small B_{OC} distortion leads to small band gap [Fig. 5(d)].

Figure 6(b) shows the average AFD distortions of NiO_6 octahedra. AFD distortions along three axes of NNO are always larger than that of SIO_1/NNO_3 superlattice, which is consistent with the larger band gap of NNO than SIO_1/NNO_3 superlattice. AFD distortions along x- and y axes decrease with the decrease of a_{IN} both in NNO and SIO_1/NNO_3 superlattice while AFD distortion along z axis first decreases and then increases with the decrease of a_{IN} both in NNO

and SIO_1/NNO_3 superlattice. Since the band gap decreases as the amplitude of AFD distortions and breathing distortion decrease, we can conclude that the decrease of octahedral rotations around x- and y axes as well as decreases of amplitude of B_{OC} distortion jointly lead to transition of SIO_1/NNO_3 superlattice from insulator to metal.

III. DISCUSSION

As proposed by Zaanen, Sawatzky, and Allen, the model called the ZSA scheme [47] correctly explained the ground state of many transition-metal oxides. This ZSA model clarified that electronic band gap depends on the ratio of the Coulomb interaction U and the charge-transfer energy Δ. Then, the insulator can be classified into the Mott-Hubbard insulator and charge-transfer insulator. In the former MIT is controlled by the Coulomb interaction U, corresponding to the process $d^n + d^n \rightarrow d^{n-1} + d^{n+1}$, while in the latter MIT is controlled by the charge-transfer energy Δ, corresponding to the process $d^n \rightarrow d^{n+1}L$ (L denotes a ligand hole). Furthermore, Mizokawa *et al.* [48,49] proposed an extension of the ZSA diagram including the negative charge-transfer insulator which is characterized by small or even negative Δ value. Strong $3d$-ligand hybridization in negative charge-transfer insulator opens a band gap which corresponds to charge fluctuations mainly of the p-p type, $d^nL + d^nL \rightarrow d^n + d^nL^2$. The SIO_1/NNO_3 superlattice is the negative charge-transfer insulator and the MIT in superlattice is induced by the strong hybridizations between $O-2p$ and $Ni-3d$ states. The insulating ground state of SIO_1/NNO_3 superlattice is characterized by a split of the electronic states of two different Ni sublattices, which possess similar amounts of charge but distinct magnetic moments. The high-spin state Ni atoms located in the center of the larger NiO_6 octahedra possess 1.23 μB magnetic moment and correspond to the $d^{8+\delta}$ state (considering the charge transfer from Ir atoms to Ni atoms). The low-spin state Ni atoms located in the center of the smaller NiO_6

octahedra possess 0.53 μB magnetic moment and correspond to the $d^{8+\delta}L^2$ state. The low-spin state Ni atoms also have a fully occupied t_{2g}^6 shell and share about two ligand holes from the surrounding oxygen octahedron. For the metal state, the difference in two Ni sublattices diminishes and two localized bands transition to a continuum of states, leading to the closing of the band gap.

IV. SUMMARY

In summary, we investigated the magnetic and electronic properties of SIO_1/NNO_3 superlattice under strain by first-principles methods and analyzed the structural distortion by symmetry-adapted mode analysis. The ground state of the superlattice is semiconducting with T-type AFM ordering, breathing distortion, and octahedra AFD distortions. At compressive strain, the octahedra breathing distortion and octahedra AFD distortions in superlattice are reduced, leading to a MIT at -1.8% strain. We further found that the breathing distortion couples with T-AFM ordering, which implies that the breathing mode is the degree of freedom to tune the magnetic properties. Our results shed light on the mechanism of MIT nickelate and give insights into the coupling between magnetic order and structural distortions.

[1] M. Imada, A. Fujimori, and Y. Tokura, Metal–insulator transitions, Rev. Mod. Phys. **70**, 1039 (1998).

[2] N. F. Mott, Metal–insulator transitions, Rev. Mod. Phys. **40**, 677 (1968).

[3] K. E. Smith and V. E. Henrich, Photoemission study of composition- and temperature-induced metal-insulator transitions in Cr-doped V_2O_3, Phys. Rev. B **50**, 1382 (1994).

[4] G. G. Guzmán-Verri, R. T. Brierley, and P. B. Littlewood, Cooperative elastic fluctuations provide tuning of the metal–insulator transition, Nature (London) **576**, 429 (2019).

[5] B. J. Kim, Hosub Jin, S. J. Moon, J.-Y. Kim, B.-G. Park, C. S. Leem, Jaejun Yu, T. W. Noh, C. Kim, S.-J. Oh, J.-H. Park, V. Durairaj, G. Cao, and E. Rotenberg, Novel $J_{eff} = 1/2$ Mott state induced by relativistic spin-orbit coupling in Sr_2IrO_4, Phys. Rev. Lett. **101**, 076402 (2008).

[6] A. Mercy, J. Bieder, J. Íñiguez, and P. Ghosez, Structurally triggered metal-insulator transition in rare-earth nickelates, Nat. Commun. **8**, 1677 (2017).

[7] H. Park, A. J. Millis, and C. A. Marianetti, Site-selective Mott transition in rare-earth-element nickelates, Phys. Rev. Lett. **109**, 156402 (2012).

[8] Y. Kohsaka, C. Taylor, K. Fujita, A. Schmidt, C. Lupien, T. Hanaguri, M. Azuma, M. Takano, H. Eisaki, H. Takagi, S. Uchida, and J. C. Davis, An intrinsic bond-centered electronic glass with unidirectional domains in underdoped cuprates, Science **315**, 1380 (2007).

[9] M. J. Lawler, K. Fujita, J. Lee, A. R. Schmidt, Y. Kohsaka, C. K. Kim, H. Eisaki, S. Uchida, J. C. Davis, J. P. Sethna, and E.-A. Kim, Intra-unit-cell electronic nematicity of the high-Tc copper-oxide pseudogap states, Nature (London) **466**, 347 (2010).

[10] Z. Qiu, D. Hou, J. Barker, K. Yamamoto, O. Gomonay, and E. Saitoh, Spin colossal magnetoresistance in an antiferromagnetic insulator, Nat. Mater. **17**, 577 (2018).

[11] Y. Tokura, Critical features of colossal magnetoresistive manganites, Rep. Prog. Phys. **69**, 797 (2006).

[12] M. Chandler Bennett, G. Hu, G. Wang, O. Heinonen, P. R. C. Kent, J. T. Kroge, and P. Ganesh, Origin of metal-insulator transitions in correlated perovskite metals, Phys. Rev. Res. **4**, L022005 (2022).

[13] S. Zhang and G. Galli, Understanding the metal-to-insulator transition in $La_{1-x}Sr_xCoO_{3-\delta}$ and its applications for

neuromorphic computing, npj Comput. Mater. **6**, 170 (2020).

[14] S. Middey, J. Chakhalian, P. Mahadevan, J. W. Freeland, A. J. Millis, and D. D. Sarma, Physics of ultrathin films and heterostructures of rare-earth nickelates, Annu. Rev. Mater. Res. **46**, 305 (2016).

[15] M. N. Grisolia, J. Varignon, G. Sanchez-Santolino, A. Arora, S. Valencia, M. Varela, R. Abrudan, E. Weschke, E. Schierle, J. E. Rault, J.-P. Rueff, A. Barthélémy, J. Santamaria, and M. Bibes, Hybridization-controlled charge transfer and induced magnetism at correlated oxide interfaces, Nat. Phys. **12**, 484 (2016).

[16] M. L. Medarde, Structural, magnetic and electronic properties of RNiO$_3$ perovskites, (R = rare earth), J. Phys.: Condens. Matter **9**, 1679 (1997).

[17] G. Catalan, Progress in perovskite nickelate research, Phase Transitions **81**, 729 (2008).

[18] J. Varignon, M. N. Grisolia, J. Íñiguez, A. Barthélémy, and M. Bibes, Complete phase diagram of rare-earth nickelates from first-principles, npj Quantum Mater. **2**, 21 (2017).

[19] J. B. Torrance, P. Lacorre, A. I. Nazzal, E. J. Ansaldo, and Ch. Niedermayer, Systematic study of insulator-metal transitions in perovskites RNiO$_3$(R = Pr, Nd, Sm, Eu) due to closing of charge-transfer gap, Phys. Rev. B **45**, 8209(R) (1992).

[20] I. Vobornik, L. Perfetti, M. Zacchigna, M. Grioni, G. Margaritondo, J. Mesot, M. Medarde, and P. Lacorre, Electronic-structure evolution through the metal-insulator transition in RNiO$_3$, Phys. Rev. B **60**, R8426(R) (1999).

[21] J. Shi, S. D. Ha, Y. Zhou, F. Schoofs, and S. Ramanathan, A correlated nickelate synaptic transistor, Nat. Commun. **4**, 2676 (2013).

[22] J. A. Alonso, M. J. Martínez-Lope, M. T. Casais, M. A. G. Aranda, and M. T. Fernández-Díaz, Metal-insulator transitions, structural and microstructural evolution of RNiO$_3$ (R = Sm, Eu, Gd, Dy, Ho, Y) perovskites: Evidence for room-temperature charge disproportionation in monoclinic HoNiO$_3$ and YNiO$_3$, J. Am. Chem. Soc. **121**, 4754 (1999).

[23] J. A. Alonso, M. J. Martínez-Lope, M. T. Casais, J. L. García-Muñoz, and M. T. Fernández-Díaz, Room-temperature monoclinic distortion due to charge disproportionation in RNiO$_3$perovskites with small rare-earth cations (R = Ho, Y, Er, Tm, Yb, and Lu): A neutron diffraction study, Phys. Rev. B **61**, 1756 (2000).

[24] J. A. Alonso, J. L. García-Muñoz, M. T. Fernández-Díaz, M. A. G. Aranda, M. J. Martínez-Lope, and M. T. Casais, Charge disproportionation in RNiO$_3$ perovskites: Simultaneous metal-insulator and structural transition in YNiO$_3$, Phys. Rev. Lett. **82**, 3871 (1999).

[25] J. A. Alonso, M. J. Martínez-Lope, M. T. Casais, J. L. García-Muñoz, M. T. Fernández-Díaz, and M. A. G. Aranda, High-temperature structural evolution of RNiO$_3$ (R = Ho, Y, Er, Lu) perovskites: Charge disproportionation and electronic localization, Phys. Rev. B **64**, 094102 (2001).

[26] J. L. García-Muñoz, J. Rodríguez-Carvajal, and P. Lacorre, Neutron-diffraction study of the magnetic ordering in the insulating regime of the perovskites RNiO$_3$ R = Pr and Nd), Phys. Rev. B **50**, 978 (1994).

[27] J. L. García-Muñoz, J. Rodríguez-Carvajal, P. Lacorre, and J. B. Torrance, Neutron-diffraction study of RNiO$_3$ (R = La, Pr,

Nd, Sm): Electronically induced structural changes across the metal-insulator transition, Phys. Rev. B **46**, 4414 (1992).

[28] A. Muñoz, J. A. Alonso, M. J. Martínez-Lope, and M. T. Fernández-Díaz, On the magnetic structure of DyNiO$_3$, J. Solid State Chem. **182**, 1982 (2009).

[29] M. T. Fernández-Díaz, J. A. Alonso, M. J. Martínez-Lope, M. T. Casais, and J. L. García-Muñoz, Magnetic structure of the HoNiO$_3$ perovskite, Phys. Rev. B **64**, 144417 (2001).

[30] A. Hampel and C. Ederer, Interplay between breathing mode distortion and magnetic order in rare-earth nickelates RNiO$_3$ within DFT + U, Phys. Rev. B **96**, 165130 (2017).

[31] D. I. Badrtdinov, A. Hampe, and C. E. Dreyer, Interplay between breathing-mode distortions and magnetic order in rare-earth nickelates from ab initio magnetic models, Phys. Rev. B **104**, 054403 (2021).

[32] G. Kresse and J. Furthmuller, Efficient iterative schemes for ab initio total-energy calculations using a plane-wave basis set, Phys. Rev. B **54**, 11169 (1996).

[33] G. Kresse and J. Furthmuller, Efficiency of *ab-initio* total energy calculations for metals and semiconductors using a plane-wave basis set, Comput. Mater. Sci. **6**, 15 (1996).

[34] G. Kresse and D. Joubert, From ultrasoft pseudopotentials to the projector augmented-wave method, Phys. Rev. B **59**, 1758 (1999).

[35] P. E. Blöchl, Projector augmented-wave method, Phys. Rev. B **50**, 17953 (1994).

[36] J. P. Perdew, A. Ruzsinszky, G. I. Csonka, O. A. Vydrov, G. E. Scuseria, L. A. Constantin, X. Zhou, and K. Burke, Restoring the density-gradient expansion for exchange in solids and surfaces, Phys. Rev. Lett. **100**, 136406 (2008).

[37] V. I. Anisimov, J. Zaanen, and O. K. Andersen, Band theory and Mott insulators: Hubbard U instead of Stoner I, Phys. Rev. B **44**, 943 (1991).

[38] A. I. Liechtenstein, V. I. Anisimov, and J. Zaanen, Density-functional theory and strong interactions: Orbital ordering in Mott-Hubbard insulators, Phys. Rev. B **52**, R5467(R) (1995).

[39] W. Guo, D. X. Ji, Z. B. Gu, J. Zhou, Y. F. Nie, and X. Q. Pan, Engineering of octahedral rotations and electronic structure in ultrathin SrIrO$_3$ films, Phys. Rev. B **101**, 085101 (2020).

[40] B. Kim, P. Liu, and C. Franchini, Dimensionality-strain phase diagram of strontium iridates, Phys. Rev. B **95**, 115111 (2017).

[41] S. Prosandeev, L. Bellaiche, and J. Íñiguez, *Ab initio* study of the factors affecting the ground state of rare-earth nickelates, Phys. Rev. B **85**, 214431 (2012).

[42] L. Binci, M. Kotiuga, I. Timrov, and N. Marzari, Hybridization driving distortions and multiferroicity in rare-earth nickelates, Phys. Rev. Res. **5**, 033146 (2023).

[43] D. Orobengoa, C. Capillas, M. I. Aroyo, and J. M. Perez-Mato, AMPLIMODES: symmetry-mode analysis on the Bilbao Crystallographic Server, J. Appl. Crystallogr. **42**, 820 (2009).

[44] J. M. Perez-Mato, D. Orobengoa, and M. I. Aroyo, Mode crystallography of distorted structures, Acta Crystallogr. Sect. A **66**, 558 (2010).

[45] G. J. MacDougall, H. M. Christen, W. Siemons, M. D. Biegalski, J. L. Zarestky, S. Liang, E. Dagotto, and S. E. Nagler, Antiferromagnetic transitions in tetragonal-like BiFeO$_3$, Phys. Rev. B **85**, 100406(R) (2012).

[46] O. Diéguez, O. E. González-Vázquez, J. C. Wojdeł, and J. Íñiguez, First-principles predictions of low-energy phases of multiferroic $BiFeO_3$, Phys. Rev. B **83**, 094105 (2011).

[47] J. Zaanen, G. A. Sawatzky, and J. W. Allen, Band gaps and electronic structure of transition-metal compounds, Phys. Rev. Lett. **55**, 418 (1985).

[48] T. Mizokawa, H. Namatame, A. Fujimori, K. Akeyama, H. Kondoh, H. Kuroda, and N. Kosugi, Origin of the band gap in the negative charge-transfer-energy compound $NaCuO_2$, Phys. Rev. Lett. **67**, 1638 (1991).

[49] T. Mizokawa, A. Fujimori, H. Namatame, K. Akeyama, and N. Kosugi, Electronic structure of the local-singlet insulator $NaCuO_2$, Phys. Rev. B **49**, 7193 (1994).